Nano Research

Open Access

Research Article

Constructing efficient electromagnetic interference shielding and Joule heating wood by crosslinking MXene nanosheets with a regenerated cellulose network

Peiru Wang§, Xiaofei Dong§, Zixuan Yang, Xueqin Fan, Yingying Liu, Yaoxing Wang, Jianfu Tang, Peng Jiao, Xueqi Li, Quankuo Zhang, Xinyuan Zhang, Ran Yin, and Wentao Gan ✉

Key Laboratory of Bio-based Material Science & Technology (Ministry of Education), Northeast Forestry University, Harbin 150040, China
§ Peiru Wang and Xiaofei Dong contributed equally to this work.

Cite this article: *Nano Research*, **2026**, *19*, 94908528. https://doi.org/10.26599/NR.2026.94908528

ABSTRACT: MXenes have emerged as highly promising candidates for electromagnetic interference (EMI) shielding. However, achieving strong interfacial adhesion of MXene nanosheets within substrate materials without applying adhesives remains challenging. To address the demand for functional coatings with integrated wear resistance, we fabricated a regenerated wood-MXene (RW-M) by creating a dense, three-dimensional (3D) nanocellulose network from partially dissolved wood surface cellulose to anchor MXene nanosheets. The ingenious structural design strategy via *in-situ* dissolved and regenerated of delignified wood surface cellulose constructs a cross-linked nanocellulose network, providing rich hydrogen binding sites for functional MXene nanosheets. After densification, the MXene nanosheets bond tightly with the delignified wood surface, significantly enhancing the mechanical stability. The composite achieves an exceptional EMI shielding effectiveness (SE) of 45 dB in the X-band (8.2–12.4 GHz) at a thin thickness of 0.35 mm, and maintains a stable SE of 39–41 dB after 1000 abrasion cycles, which is attributed to the robust interfacial bonding and mechanical interlocking. Moreover, the RW-M also exhibits outstanding Joule heating performance, reaching 115 °C with 5 V of applied voltage. This work provides a green strategy for designing EMI shielding materials, showing great potential for applications in decoration, building, and advanced thermal management systems.

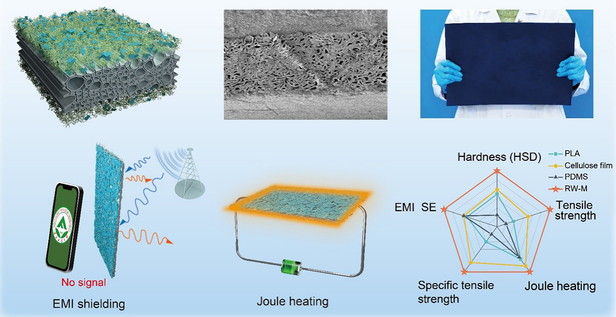

KEYWORDS: regenerated cellulose, MXene, electromagnetic interference (EMI) shielding, Joule heating, wear resistance

1 Introduction

In the current digital age, the pervasive use of electronic devices has greatly improved social efficiency and convenience. However, these devices also generate electromagnetic interference (EMI) and radiation during operation, leading to equipment malfunctions and data transmission interruptions [1–4]. Prolonged exposure to such emissions may threaten human health by adversely affecting the nervous, cardiovascular, and immune system [5–7]. These concerns have spurred the need for high-performance EMI shielding materials. In parallel, there is an increasing demand for rapid thermal management across various fields, including smart homes and aerospace [8, 9]. An ideal solution involves multifunctional materials that integrate efficient EMI shielding with Joule heating capabilities to meet the diverse performance requirements of modern technologies [10, 11].

Traditional metal-based EMI shielding materials possess exceptional electrical conductivity and superior EMI shielding performance, yet their high density, energy-intensive processing, and vulnerability to corrosion significantly restrict their use in lightweight equipment [12]. In contrast, polymers and carbon-based composites offer benefits such as light weight, chemical robustness, weather resistance, and favorable physical properties [13–17]. However, their complex synthesis routes often lead to high costs and poor recyclability. Recently, two-dimensional transition metal carbides/nitrides (MXenes) have attracted significant

Received: November 27, 2025; **Revised:** January 29, 2026
Accepted: February 3, 2026

✉Address correspondence to wtgan@nefu.edu.cn

attention for EMI shielding, owing to their high electrical conductivity and large aspect ratio [18–24]. Nevertheless, the weak interfacial adhesion between MXene nanosheets complicates their assembly into macrostructures, limiting its practical applications. To address this issue, various polymers such as polyvinyl alcohol (PVA) [25, 26], aromatic polyamides (ANF) [27, 28], sodium alginate [29, 30], and epoxy resins [31, 32] have been incorporated through covalent/non-covalent bonds, coordination, or esterification. These methods promote crosslinking or the formation of porous and sandwich architectures, enhancing the interfacial strength and mechanical properties of MXene-based materials. Despite these advances, the reliance on non-renewable polymer matrices poses a significant barrier to developing high-performance, large-area shielding materials that align with green and sustainable objectives.

Cellulose, as an inherently green and sustainable material, exhibits a high specific surface area and abundance of hydroxyl groups, endowing it with favorable chemical reactivity [33, 34]. When exfoliated into cellulose nanofibers, it can form robust supramolecular networks with MXene through hydrogen bonding, van der Waals interactions, and physical entanglement, thereby facilitating the construction of stable functional composites [35]. However, conventional nano-fibrillation methods such as mechanical milling [36] and 2,2,6,6-tetramethylpiperidine-1-oxyl (TEMPO)-mediated oxidation [37] often involve high energy consumption, toxic chemicals, or complex processing. Recently, there has been significant progress in developing multifunctional wood materials. Innovative strategies such as cell wall engineering [38], biomechanochemical processing [39], and localized moisture gradient control [40] have successfully transformed natural wood and bamboo into high-strength, three-dimensional (3D)-moldable structural materials. However, in the case of natural cellulose-based substrates like wood, a promising green material for building and decorative applications, the weak interfacial adhesion between the biobased matrix and inorganic conductive MXene coatings leads to progressive detachment under external stress or prolonged use, resulting in significant performance degradation [41, 42]. Therefore, the development of high-performance MXene/wood composites that combine efficient processing with strong interfacial stability remains a critical and ongoing challenge.

In this study, we developed an ingenious structural design strategy to construct the robust and multifunctional regenerated wood-MXene (RW-M) through forming permeable, highly entangled nanocellulose network on the wood surface by *in situ* cellulose dissolution-regeneration, enabling effective MXene anchoring and interfacial stabilization. As shown in Fig. 1(a), the exposed cellulose fibers are dissolved and regenerated into a dense 3D nanocellulose network with high permeability, hygroscopicity, and intricately entangled structure. MXene nanosheets are subsequently introduced and firmly anchored within this intricately entangled cellulose framework via multiscale hydrogen bonding and chemical interactions. Mechanical compression is then applied at room temperature to densify the composite, forming an exceptionally stable MXene coating with superior interfacial bonding and robust wear resistance.

The resulting RW-M demonstrates a remarkable EMI shielding

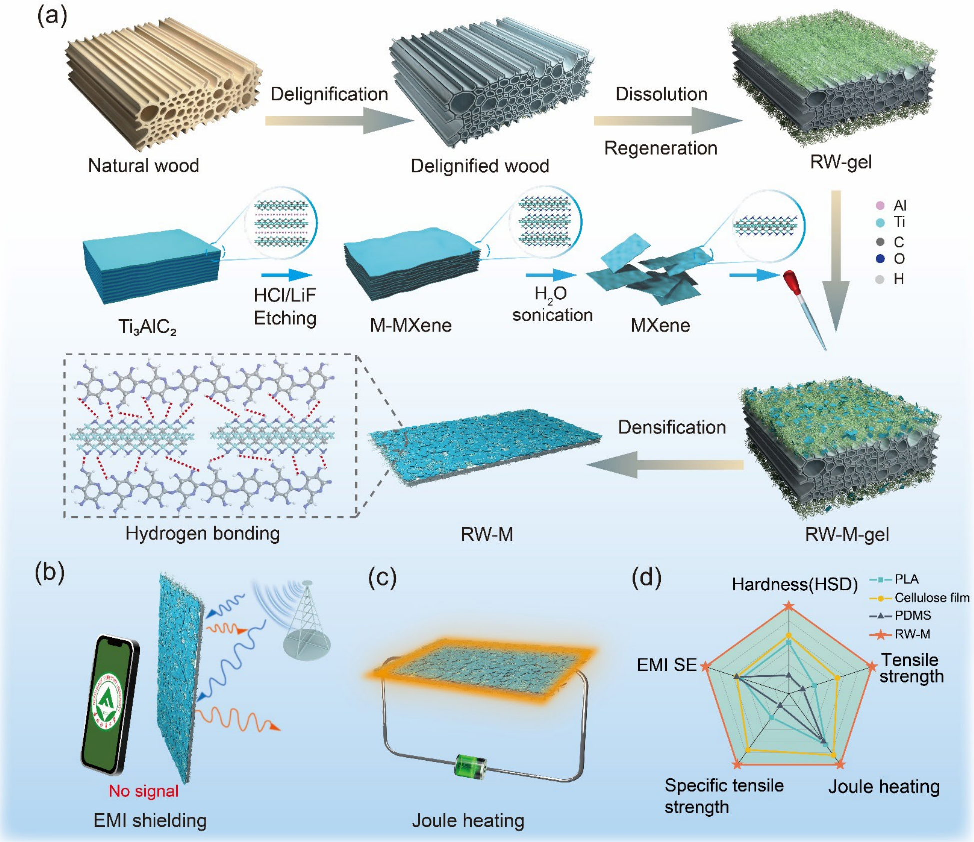

Figure 1 Preparation and multifunctional applications of RW-M. (a) Schematic of the synthesis process of RW-M and MXene. (b) Schematic illustration of the EMI shielding of RW-M. (c) Schematic illustration of low-voltage Joule heating of RW-M. (d) Comparison of specific tensile strength, Joule heating, tensile strength, EMI SE and hardness of the RW-M with PLA, cellulose film, and PDMS (Table S1 in the ESM).

effectiveness (SE) of 45 dB in the X-band (8.2–12.4 GHz) at a thin thickness of 0.35 mm (Fig. 1(b)). It also exhibits excellent low-voltage Joule heating characteristics, rapidly reaching a steady-state surface temperature of 40 °C at only 1.5 V (Fig. 1(c)). The hydrogen-bonded cross-linking between MXene and cellulose network significantly enhances the mechanical properties, yielding a tensile strength of 367 MPa and an elastic modulus of 7.8 GPa. Moreover, the RW-M retains high EMI shielding and Joule heating performance even after 1000 abrasion cycles, underscoring superior interface stability. Benefiting from the natural hierarchical structure of wood and the high interfacial compatibility between cellulose nanofibers and MXene nanosheets, RW-M shows superior EMI SE and mechanical properties than those of the composites made up by poly lactic acid (PLA), cellulose film and polydimethylsiloxane (PDMS) (Fig. 1(d) and Table S1 in the Electronic Supplementary Material (ESM)). Through the integration of regenerated wood and MXene, this work effectively addresses the intrinsic mechanical fragility of MXene and improves its interfacial compatibility. The RW-M thus represents a promising multifunctional material platform for applications in construction, smart homes, and aerospace, offering new insights for designing high-performance multifunctional composites.

2 Experimental

2.1 Materials and chemicals

Poplar wood for this experiment was purchased from a timber factory in Shandong Province, China. Acetic acid was obtained from Tianli Chemical Reagent Co., Ltd. Dimethylacetamide (DMAc, > 99%) and ethanol were supplied by Fu Yu Fine Chemical Co., Ltd. Sodium chlorite ($NaClO_2$, 80%) and lithium chloride (LiCl, > 99%) were purchased from Shanghai Aladdin Biochemical Technology Co., Ltd. Deionized water was used throughout all wood processing procedures. Ti_3AlC_2 was procured from 11 Technology Co., Ltd. in Jilin Province. Hydrochloric acid (analytical grade) was provided by Guangdong Xilong Science Co., Ltd., and lithium fluoride (LiF, > 99%) was sourced from Shanghai McLean Biochemical Technology Co., Ltd.

2.2 Preparation of Ti_3C_2T MXene nanosheets

LiF (3.2 g) was dissolved in 40 mL of HCl (9 M) in a polytetrafluoroethylene reactor to get a homogenous solution under stirring at room temperature. Subsequently, Ti_3AlC_2 (2 g) was gradually added to the LiF/HCl solution to obtain the mixture. The mixture was then reacted at 40 °C in a constant temperature water bath for 24 h. After reaction, the mixture was transferred to a 50 mL centrifuge tube and washed repeatedly with deionized water. The acidic supernatant was removed by repeated centrifugation (3500 rpm, 5 min) until the pH reached 5, yielding a purified multilayer MXene (M-MXene). The obtained M-MXene was re-dispersed in deionized water and sonicated in an ice bath for 2 h to promote exfoliation into monolayers. Finally, the dispersion was centrifuged at 6000 rpm for 30 min, and the supernatant was collected to obtain a single-layer MXene dispersion.

2.3 Preparation of *in situ* partial dissolution of cellulose on the surface of wood

First, poplar veneers were immersed in a 5 wt.% $NaClO_2$ solution (pH = 4.6, adjusted with acetic acid) for 4 h, and then rinsed thoroughly with deionized water to remove chemical residues obtain delignified wood. Subsequently, the delignified wood was immersed in anhydrous ethanol to exchange out the internal water and then placed in DMAc for activation. Finally, the activated wood sample was placed in an 8 wt.% DMAc/LiCl solution for 1 h, after which it was regenerated in water and freeze-dried for 12 h to obtain the RW-gel.

2.4 Fabrication process of RW-M

MXene solution (20 $mg\cdot mL^{-1}$) was applied dropwise using a dropper and spread evenly over the dried RW-gel veneer. The sample was then uniaxially compressed at room temperature with a mechanical press under a pressure of 2000 psi for 24 h to obtain RW-M. The loading of MXene (defined as mass per unit of substrate area, $mg\cdot cm^{-2}$) was determined by weighing the MXene after it had completely dried. In this study, we investigated the performance of RW-M at representative loadings of 4.5 and 9.6 $mg\cdot cm^{-2}$.

2.5 Fabrication of MXene films, natural wood-MXene, and delignified wood-MXene

Pure MXene films with about 40 mm diameter were synthesized via vacuum filtration of 10–15 mL aqueous MXene dispersion through a hydrophilic membrane. Delignified wood-MXene and natural wood-MXene were prepared by drop-coating identical MXene solutions (equivalent concentration and volume to those used in RW-M) onto their respective wood substrates. Subsequently, the delignified wood-MXene was mechanically compressed under the same conditions as RW-M, while the natural wood-MXene was left uncompressed after coating.

2.6 Materials characterization

The microscopic morphology of wood samples was characterized by optical microscope (Mingmei, MJ31), scanning electron microscope (SEM, HITACHI TM3030) combined with an energy dispersive spectrometer (EDS), and transmission electron microscope (TEM, FEI Talos F200X). X-ray diffraction analysis (XRD, SHIMADZU 6100) was conducted at a scan rate of 10 $°\cdot min^{-1}$ from 5° to 80°. The holocellulose content in the wood samples was obtained by means of a sodium chlorite and acetic acid treatment for 1 h at 90 °C according to ASTM D-1104 standard (ASTM International, 1978). Acid-insoluble lignin and α-cellulose content in the wood samples were measured in accordance with TAPPI T 429 and TAPPI T 222 standards, respectively. Fourier transform infrared (FTIR) spectrometer (Magna-IR 560, Nicolet) was used to characterize the FTIR spectrum of samples. The spectra were collected from 4000 to 800 cm^{-1} at 4 cm^{-1} resolution. The surface chemical properties and composition of samples were characterized by X-ray photoelectron spectroscopy (XPS, Escalab 250Xi, Thermo Fisher).

2.7 Performance tests

The mechanical tensile tests of samples were performed on a universal testing machine (Suns, UTM2503) with loading speed of 1 $mm\cdot min^{-1}$. The average Shore D hardness of samples was evaluated by Shore D Durometer. Wear testing was conducted using a Steel Wool Abrasion Tester (Model: ZJ-339-GSR) with 80-grit sandpaper under 250 g load. The EMI SE was calculated from the scattering parameters measured with a two-port vector network analyzer (VNA, P5004A, Keysight) via a rectangular waveguide adapter in the X-band (8.2–12.4 GHz). Tesla coil (Anhui Lightning Wholesale Factory), served as the electromagnetic shielding emission source. The change of temperature was recorded via an infrared thermal imager (Testo 869) in real time. A DC power supply (PaiSheng, Model: PS-3010D) provided a constant voltage to the system. Linear sweep voltammetry (LSV) was performed on an electrochemical workstation (Model CHI760E, Shanghai Chen hua Instrument Co., Ltd., China).

3 Results and discussion

3.1 Morphological and structural features of RW-M

RW-M was prepared by delignification and *in-situ* assembly on the substrate of natural poplar veneer (see Materials and Methods for details). Natural wood with the hierarchical porous structure displays numerous irregular 3D polygonal cell cavities in the cross-section (Figs. S1(a) and S1(b) in the ESM) and aligned tracheids and fibers in the radial section (Fig. S1(c) in the ESM). Initially, rotary-cut natural poplar wood is immersed in a $NaClO_2$ solution, during which the brown wood is delignified into the white cellulose-rich scaffold (Figs. 2(a) and 2(b)). The lignin deposited in the middle lamella and cell corners of middle lamella are effectively eliminated, resulting in a loosening of the wood cell wall and exposing a large number of cellulose fibers (Fig. S2 in the ESM). SEM confirms the preservation of the original porous structure in delignified wood, while chemical analysis reveals a new composition of 69.6% cellulose and 28.8% hemicellulose, with lignin minimized to 1.8% (Fig. S3 in the ESM). The disappearance of the characteristic peaks at 1593, 1506, and 1458 cm^{-1} in the FTIR spectra further supports the removal of lignin (Fig. S4 in the ESM). Due to the increased porosity of the cell wall and more free hydroxyl groups exposed on its surface, the chemical accessibility of delignified wood is greatly enhanced, which is an essential prerequisite for the construction of nanocellulose networks. Subsequently, delignified wood is immersed in LiCl/DMAc solution, utilizing OH-Cl^- intermolecular interactions to disrupt OH–O hydrogen bonds between cellulose chains, while Li^+ cations then bind to the carbonyl oxygen of DMAc to form Li^+(DMAc) complexes, maintaining electrical equilibrium along with Cl^- ions (Fig. 2(c)) [43, 44]. Compared to untreated delignified wood (Fig. S5 in the ESM), soaked delignified wood is swollen and partially solubilized, where the dissolved cellulose solution covers the surface of the cellulose framework (Fig. 2(d)). Upon regeneration in water, the intra- and inter-molecular hydrogen bonds are reorganized and the dissolved cellulose chains coagulate into a regenerated nanocellulose network, which is assembled with the preserved porous structure of wood to form a RW-gel (Figs. 2(e)–2(h)).

Based on the chemical etching principle, a mixture of HCl and LiF is used to selectively etch the Al layer from the precursor

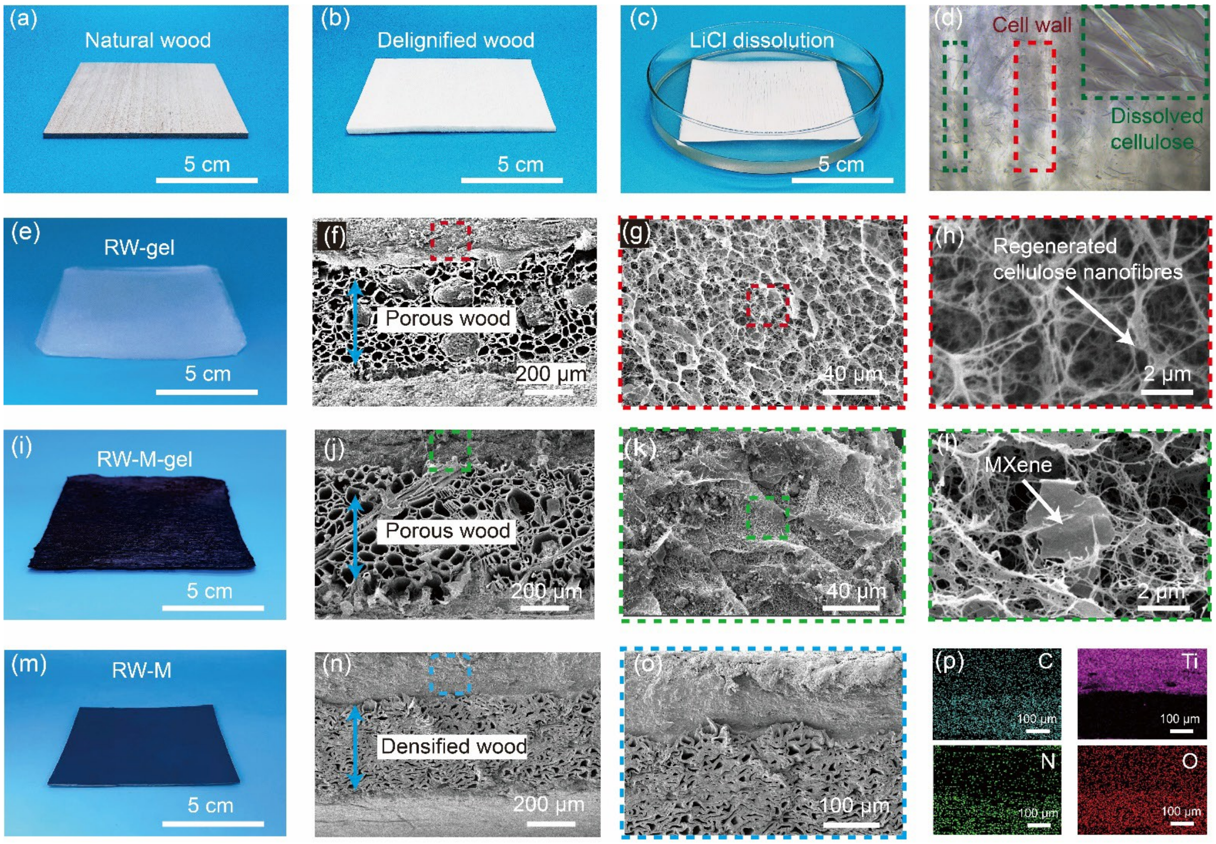

Figure 2 Morphological and structural features of as-prepared wood samples. (a) Photograph of natural wood (a 2-mm-thick poplar board). (b) Photograph of the delignified wood. (c) Photograph of the wood sample dissolved in DMAc/LiCl solution. (d) Optical microscope image of delignified wood after dissolution treatment, revealing an intact wood cellulose framework and a completely dissolved cellulose solution. (e) Photograph of the RW-gel. (f)–(h) Cross-sectional SEM images of the RW-gel, showing the regenerated cellulose layer on the surface and its internal 3D network structure. (i) Photograph showing RW-M-gel obtained by drip-coating RW-gel with MXene. (j)–(l) Cross-sectional SEM images of the RW-M-gel demonstrate the cross-linking and entanglement of the cellulose network with MXene nanosheets. (m) Photograph showing RW-M obtained through the densification of RW-M-gel. (n) and (o) Cross-sectional SEM images of the compressed RW-M reveal its dense laminated structure. (p) Cross-sectional EDS elemental mappings of RW-M (C, N, O, and Ti).

Ti_3AlC_2 MAX phase, producing a single-layer MXene aqueous solution (Figs. S6(a)–S6(c) in the ESM). Tyndall effect demonstrates that MXene exhibits excellent dispersibility and stability in water (Fig. S6(d) in the ESM). Vacuum filtration was employed to deposit the MXene dispersion onto a filter membrane, with SEM revealing a well-defined layered structure (Figs. S6(e) and S6(f) in the ESM). TEM and selected area electron diffraction (SAED) reveal the high crystallinity and hexagonal basal plane structure of MXene sheets, without apparent defects (Fig. S6(g) in the ESM). Atomic force microscopy (AFM) further confirms the successful preparation of monolayer MXene with uniform thickness (Fig. S6(h) in the ESM). XPS analysis confirms the presence of Ti, C, and O elements on the MXene surface, along with the presence of –OH, –F, and –O functional groups (Figs. S6(i)–S6(l) in the ESM), which enhances the hydrophilicity of MXene and improves their interfacial adhesion properties with wood substrates. Benefitting from the abundant hydrophilic hydroxyl (–OH) functional groups and dense cellulose network structure, RW-gel also represents excellent hydrophilicity (Figs. S7(a)–S7(c) in the ESM). Through drop-coating, MXene nanosheets penetrate and tightly adhere to the RW-gel cellulose skeleton, forming a homogeneous functional coating with high-density hydrogen bonding, thus yielding the RW-gel loaded MXene (RW-M-gel) (Figs. 2(i)–2(l) and Fig. S8 in the ESM).

Following mechanical compression, the sample undergoes semi-densification, which is reflected in a significant reduction in its thickness (Figs. 2(m) and 2(n)). Cross-sectional SEM images and EDS clearly reveal the robust interfacial structure of RW-M, in which the uniform distribution of titanium (Ti) verifies the continuous incorporation of MXene into the 3D nanocellulose network (Figs. 2(o) and 2(p)). The XRD pattern of RW-M exhibits a characteristic peak of the (002) plane of Ti_3C_2 MXene near 6°, confirming the successful assembly of MXene in a layered structure on the surface of RW-gel (Fig. S9 in the ESM). To gain further insight into the interfacial interactions at the molecular level, XPS was performed to confirm the coexistence of RW-gel and MXene components (Fig. S10(a) in the ESM). High-resolution XPS spectra of O 1s, C 1s, and Ti 2p (Figs. S10(b)–S10(d) in the ESM) are deconvoluted to systematically elucidate the interfacial bonding mechanism between RW-gel and MXene in RW-M. The O 1s spectrum consists of Ti–O–Ti (from MXene), C–O (from cellulose), and C–O–Ti bonds (at 530.8 eV). The presence of the C–O–Ti bond provides direct evidence for chemical bridging at the RW-M interface. In the C 1s spectrum, in addition to the characteristic cellulose components (O–C=O, C–O, and C–C), a distinct C–Ti peak is observed, further supporting the presence of interfacial chemical bonding. The Ti 2p spectrum not only shows intrinsic MXene environments (Ti–C, Ti–F, and Ti–O) but also clearly reveals the presence of Ti–O–C bonds, offering definitive evidence for covalent interfacial bonding. Consequently, the RW-M exhibits a dual cross-linked interface, which is synergistically reinforced by non-covalent bonding from the nanocellulose network and covalent Ti–O–C bond. This rationally designed interface provides a critical structural foundation for achieving enhanced mechanical and functional properties in the composite material.

3.2 EMI shielding of the RW-M

As shown in Fig. 3(a), with 4.5 mg·cm^{-2} of MXene in the RW-M, X-band EMI SE increased from 1 to 22 dB, arriving at the commercial SE value of 20 dB. When the MXene loading was increased to 9.6 mg·cm^{-2}, SE rose sharply to 45 dB. The enhanced SE results from the higher MXene content promoting the formation of additional conductive paths and more mobile charge carriers. The pure MXene film exhibited the highest EMI SE, reaching approximately 56 dB in the X-band (Fig. S11(a) in the ESM). The EMI SE of delignified wood-MXene and natural wood-MXene is about 41 dB in the X-band (Figs. S11(b) and S11(c) in the ESM). However, the multi-layered structure after semi-densification in RW-M effectively reflects and scatters electromagnetic waves (EMWs), lengthening the path and enhancing dissipation, to achieve an optimal balance between mechanical properties and EMI SE (Fig. S12 and Table S2 in the ESM). The total SE (SE_T) involved the shielding by reflection (SE_R) and absorption (SE_A). At a loading of 9.6 mg·cm^{-2}, the SE_T, SE_A, and SE_R values of RW-M are 45, 39, and 6 dB, respectively (Fig. 3(b)). Additionally, *R* (reflection) was much higher than *A* (absorption) and *T* (transmission), which indicated that reflection played a dominant role in the attenuation of the EM waves (Fig. 3(c)). For the two pieces and three pieces samples, the SE values increase from 45 to 80–100 dB. The multiple reflections and scattering between the stacked RW-M layers enhance the shielding performance (Fig. 3(d)). Moreover, since the nanocellulose network effectively protects MXene from oxidation, the samples show remarkable long-term EMI shielding stability with almost no change after several days of air exposure (Fig. 3(e)). These characteristics surpass many wood-based composite, MXene, metal and graphene shielding materials, making RW-M extremely competitive for EMI shielding (Fig. 3(f) and Table S3 in the ESM).

The EMI shielding mechanism of RW-M lies in the integration of MXene nanosheets on the RW-gel surface, where the synergistic effect of the nanosheets and the multiscale cellulose network enables efficient electromagnetic energy dissipation (Fig. 3(g)). This assembly strategy enables the MXene nanosheets to overlap, creating a complete and efficient conductive network that significantly enhances both conductive loss and polarization effects. Due to impedance mismatch caused by the abundant free electrons on the RW-M surface, part of the incident wave is promptly reflected when the EMWs reach its surface. The remaining wave penetrates the highly conductive MXene layer and interacts with charge carriers, inducing substantial ohmic loss and induced current that further dissipate the electromagnetic energy. Simultaneously, the abundant terminal functional groups and structural defects on the MXene surface act as dipole centers, leading to polarization relaxation and dielectric loss under the influence of the high-frequency electric field. In addition, the porous wood structure is transformed into a laminated dense network after compression, which forms robust interfacial connections with the conductive MXene nanosheets. This re-engineered microstructure effectively promotes multiple internal reflections and scattering of EMWs.

In order to demonstrate the outstanding EMI shielding of RW-M, we designed a practical communication scenario with two smartphones to visually evaluate its signal-blocking effectiveness in a real environment (Fig. 3(h)). First, we removed the top of a standard shielded box with shielding material on all sides and replaced it with a holey copper mesh to create a perforated shielding box. Subsequently, a smartphone was placed in the box and called with another smartphone placed outside, which resulted in successful reception of communication signals by the phone placed inside the box. However, when the holes were completely covered with RW-M and repeated dialing, the in-box phone

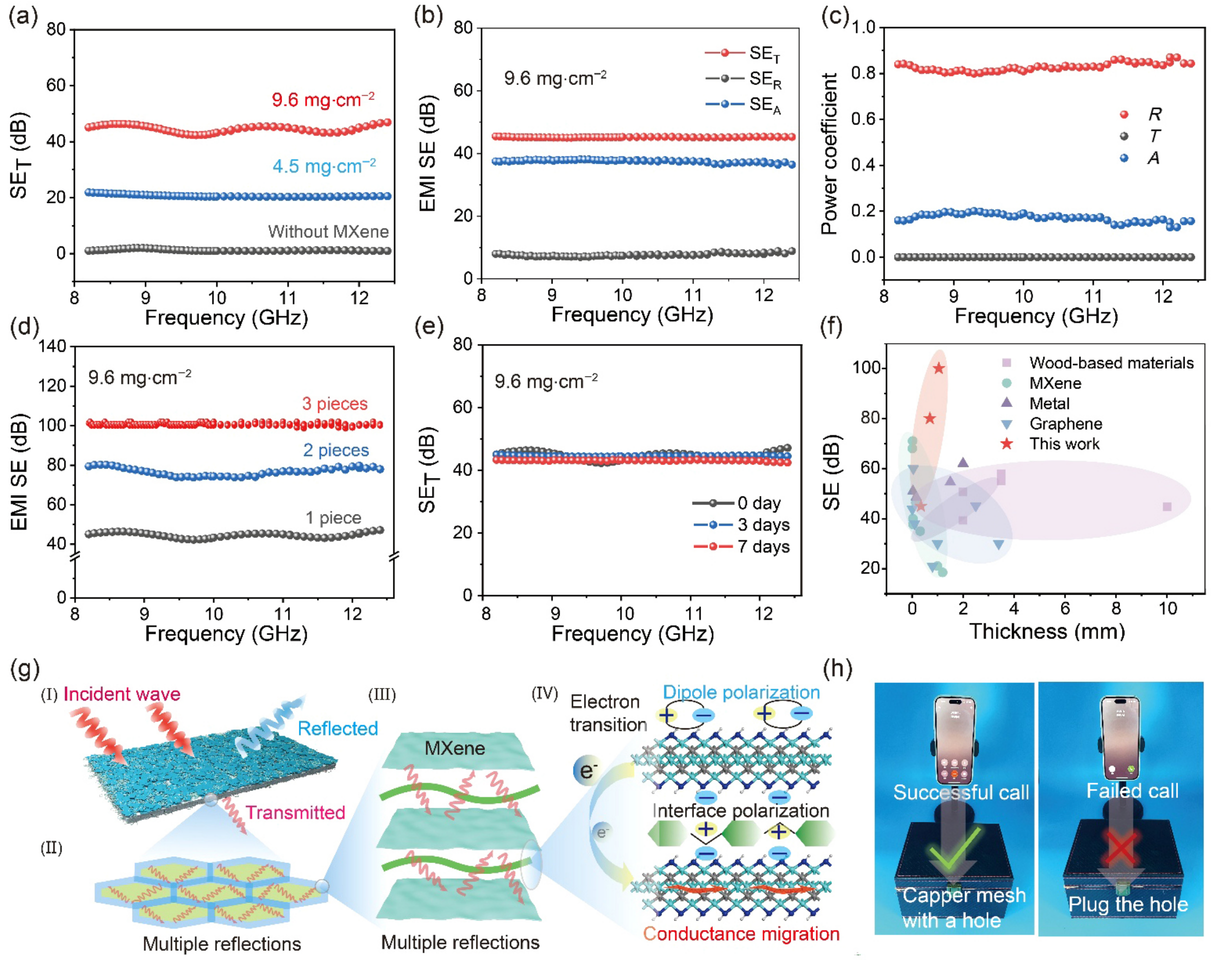

Figure 3 EMI shielding of the RW-M. (a) EMI SE of the RW-M with different MXene loadings (0, 4.5, and 9.6 mg·cm^{-2}) in the X-band. (b) Contributions of SE$_A$, SE$_R$, and SE$_T$ to the EMI SE of the RW-M with an MXene loading of 9.6 mg·cm^{-2}. (c) The corresponding average power coefficients of reflection (*R*), absorption (*A*), and transmission (*T*) for RW-M. (d) EMI SE as a function of the number of RW-M layers. (e) Evolution of EMI SE for the RW-M over time in the 8.2–12.4 GHz frequency range. (f) Comparison of the specific EMI SE of RW-M with other reported shielding materials. (g) Schematics ((I)–(IV)) illustrating the EMI shielding mechanism of the RW-M. (h) Simulated application scenario demonstrating EMI shielding for signal isolation between mobile devices.

connection was interrupted, demonstrating the effective signal shielding capability of this material. These results clearly exhibit the effective EMI shielding of RW-M, indicating its potential for applications in radiation protection and signal security.

3.3 Joule heating of RW-M

In addition to EMI shielding, RW-M also presents highly effective Joule heating characteristics, which stems from the 3D conductive cellulose network formed by MXene nanosheets within the regenerated nanocellulose. MXene nanosheets are firmly anchored in a 3D cellulose network and mechanically compressed to form a dense lamellar structure, which provides a low-resistance pathway for electron migration under applied voltage. In addition, the 3D conductive network acts as a uniformly distributed heat source, which facilitates the rapid diffusion of heat within the surface to realize rapid and uniform surface heating [45]. When an electric current is applied to RW-M, it will generate heat, functioning as a thermal management floor for regulating temperatures in indoor spaces such as offices and passenger aircraft cabins (Fig. 4(a)). Upon connection to a DC power supply via spring-loaded electrodes, the applied constant voltage induces a continuous current flow which creates a uniform thermal distribution across the material. As the temperature rises, the resistance increases and the current inside of the material continuously reduces until thermal equilibrium is achieved. The temperature changes of the RW-M under different fixed voltages are verified by infrared thermal imaging, demonstrating that it can be accurately controlled in terms of temperature and heating rate.

Figures 4(b) and 4(c) illustrate the Joule heating curves at different voltages obtained by monitoring the sample surface temperature and the corresponding temperature profiles captured via infrared thermography. In particular, operating heating devices at low voltages is critical for energy efficiency. At 1 V, the RW-M surface temperature rapidly rises from 29 to 35 °C in seconds, and with 5 V applied, the temperature can elevate to 115 °C. Fitting the temperature data to U^2 reveals a linear relationship (R^2 = 0.99), consistent with Joule heating theory, which further indicates the reliability of the experimental results (Fig. 4(d)). Given the critical importance of thermal stability for practical application, a systematic evaluation of this property was conducted on the sample surface under a fixed bias voltage of 4 V. As shown in Fig. 4(e), the RW-M exhibits outstanding operational stability, maintaining a consistent surface temperature with minimal fluctuation (±1.5 °C) throughout a continuous 3000 s test period. Furthermore, varying

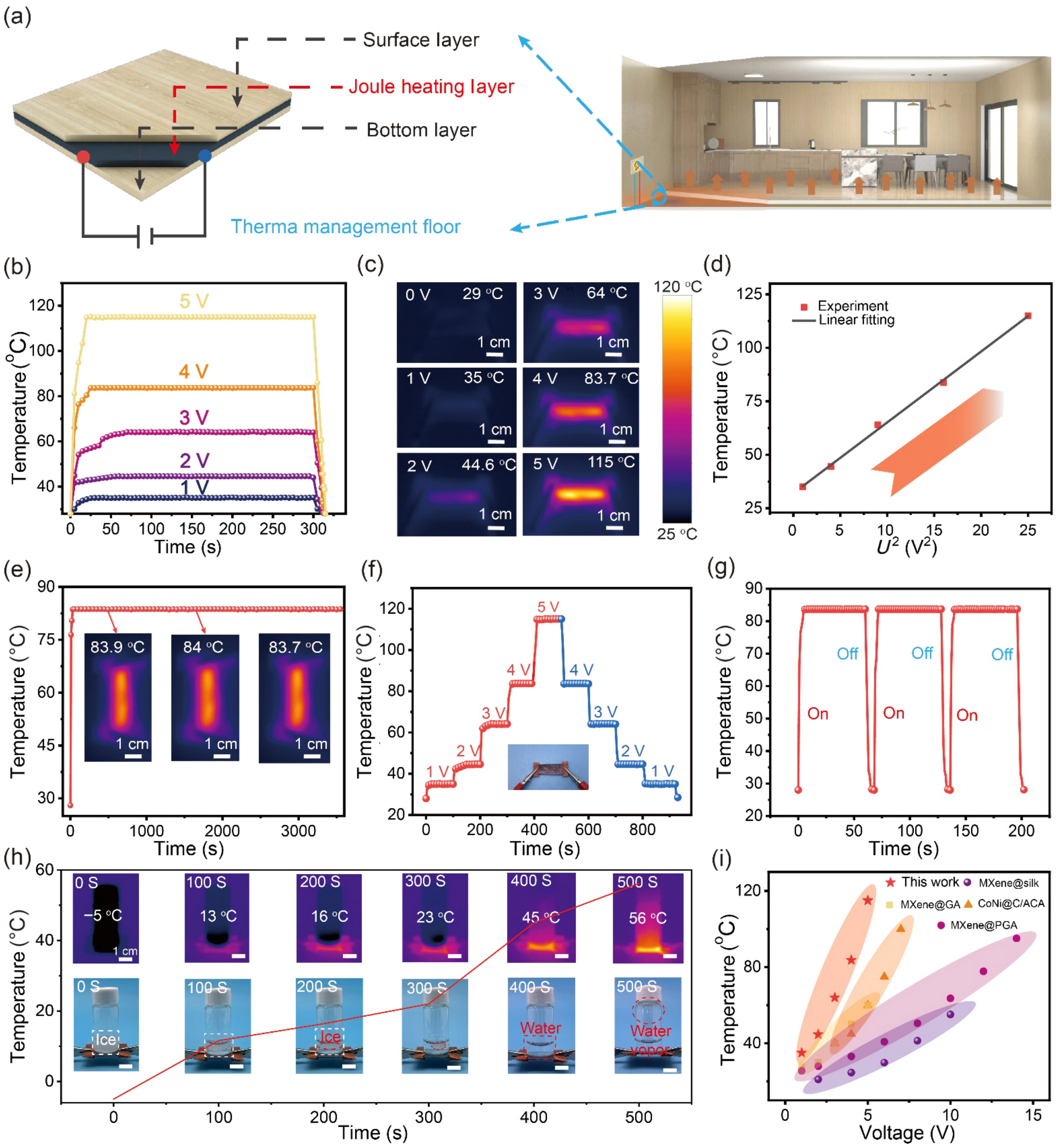

Figure 4 Application diagram of RW-M based on Joule heating characteristics. (a) Schematic diagram of the RW-M exhibiting the Joule heating effect. (b) Variation curves in surface temperature of RW-M over time under different input voltages. (c) Infrared thermal images of RW-M at various driving voltages. (d) Linear fitting of surface temperature versus U^2 based on experimental data. (e) Cyclic stability test of RW-M at 4 V. (f) Steady-state surface temperature of RW-M as a function of applied voltage. (g) Repetitive Joule heating cycles at 4 V. (h) Optical and infrared images of RW-M melting ice mass at 4 V, with its surface temperature variation curve. (i) Comparison of the Joule heating performance of RW-M with other recently reported MXene-based materials [48–51].

the applied voltage also enables to precisely regulate the surface temperature of RW-M, confirming its high electrothermal conversion efficiency and predictable thermal response (Fig. 4(f)).

We also quantitatively evaluated the cyclic Joule heating performance of the RW-M through three consecutive on/off cycles at 4 V (Fig. 4(g)). The sample exhibits rapid thermal response kinetics, reaching 83 ± 2 °C within 20 s after activation and returning to ambient temperature (25 ± 1 °C) within equivalent duration upon deactivation. Notably, no significant thermal hysteresis ($\Delta T < 3\%$) was observed across cycles, indicating the RW-M has remarkable thermal cycling stability. To further validate practical applicability, an ice-melting text was performed at constant 4 V. As shown in Fig. 4(h), the 5 mL ice mass experienced a complete phase transition at 400 s, and observable vapor condensation appeared at 500 s. At an applied voltage of 5 V, RW-M achieves a high-power density of 90.57 W·cm^{-2} and 115 °C corresponding temperature (Table S4 in the ESM), which is comparable to the currently reported leading electrothermal materials [46, 47]. In a linear sweep voltammetry test (0–5 V, 200 mV·s^{-1}), the current–voltage curve of RW-M shows excellent linearity (R^2 = 0.99), which demonstrates its highly controllable heating process (Fig. S13 in the ESM). Compared to reported electrothermal materials, RW-M exhibits superior fast, low voltage thermal response features (Fig. 4(i)). Overall, the fast response, stable cycling performance, and precise voltage–temperature correlation establish RW-M as a promising candidate for advanced thermal management systems.

3.4 Mechanical performance of RW-M

Owing to the high-density hydrogen-bonded crosslinked network and moderate compression treatment, the mechanical properties of RW-M have been significantly enhanced. The thickness has been decreased from 2 to 0.35 mm (the 83% reduction, corresponding to a fivefold increase in density), and the natural wood cell cavities have formed a dense layered structure that greatly improves the mechanical strength of the RW-M (Fig. S14 in the ESM). The tensile strength and modulus of RW-M in the longitudinal direction (L-direction) reach 367 MPa and 7.5 GPa, respectively, exceeding that of natural wood and other samples (Figs. 5(a)–5(c)). The transverse tensile (T-direction) strength of RW-M is approximately 10-fold and 4-fold of natural wood-MXene and delignified wood-MXene (Fig. 5(b)). Considering the inherently low density of cellulose, RW-M exhibits superior specific tensile strength of up to 407 MPa·cm^{-3}·g^{-1}, even surpassing many lightweight alloys (e.g., stainless steel, 4 Ni-Cr-Mo steel, Cr-Mn-Fe-Co-Ni, Mg-6Al-1Zn, Ti6Al4V, and Al alloys) (Fig. 5(d)). In addition, SEM images of the RW-M fracture surface clearly show the intertwined and densely arranged wood cell walls without visible voids (Fig. S15 in the ESM), further confirming its remarkable mechanical properties. With the rational structural design, RW-M achieves both enhancement in mechanical strength and EMI shielding performances, delivering considerably outstanding comprehensive properties compared to other wood-based, cellulose-based, polymer-based, and aramid nanofiber-based (ANF-based) shielding materials (Fig. 5(e) and Table S5 in the ESM).

In addition, RW-M is nearly 3-fold harder than natural poplar wood and outperforms several common polymer materials (Fig. 5(f)), showing excellent micromechanical properties and surface structural stability (Fig. S16 in the ESM). After 1000 abrasion cycles, RW-M exhibits minimal surface loss, whereas natural wood-MXene and delignified wood-MXene have noticeable coating damage after 200 cycles (Fig. 5(g) and Fig. S17 in the ESM). Meanwhile, EDS indicates markedly reduced Ti content in the wear areas of natural wood-MXene and delignified wood-MXene compared to RW-M (Figs. S18 and S19 in the ESM). We also

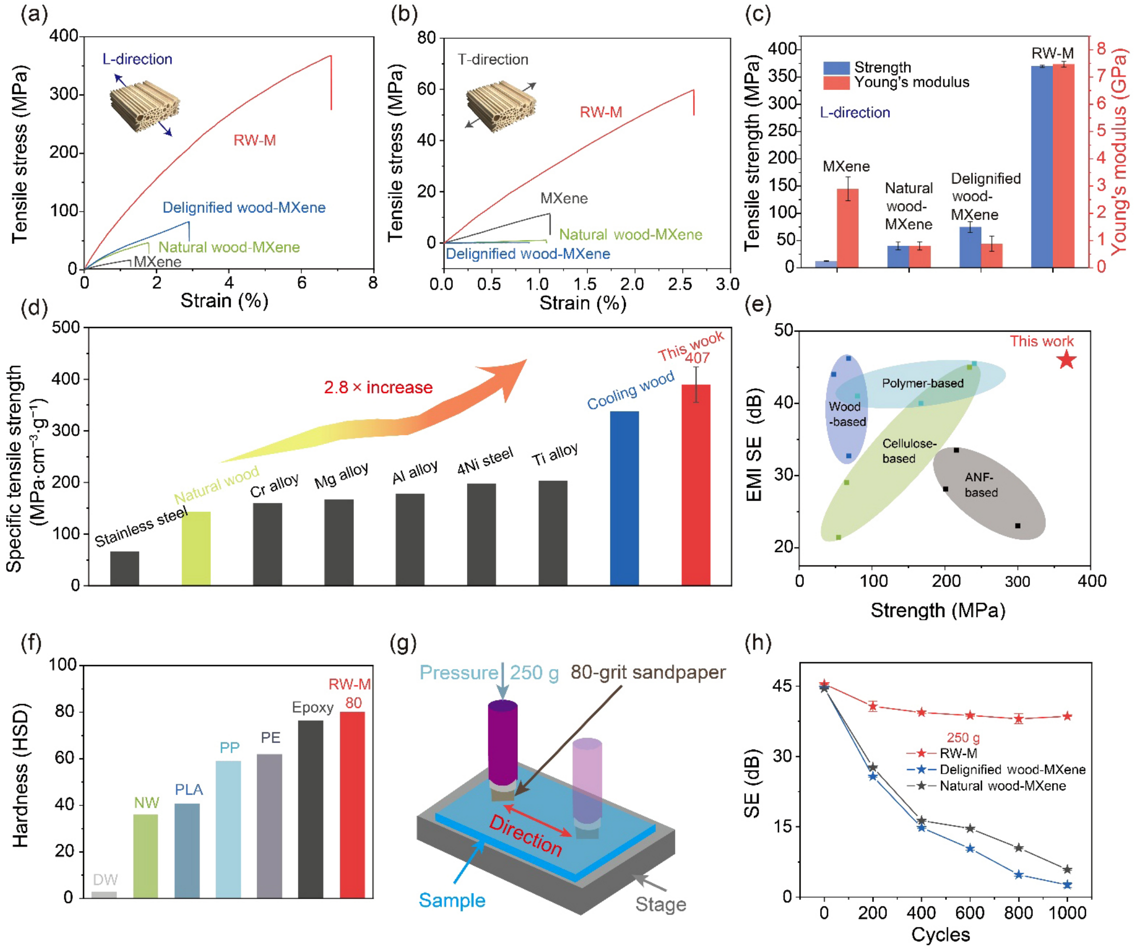

Figure 5 Mechanical performance of RW-M. (a) Tensile stress–strain curves in the L-direction of natural wood-MXene, delignified wood-MXene, and RW-M. (b) Tensile stress–strain curves in the T-direction of natural wood-MXene, delignified wood-MXene, and RW-M. (c) Comparison of tensile strength and modulus in the L-direction of the three materials. (d) Specific tensile strength of RW-M compared with metals and lightweight structural materials [52–57]. (e) Correlation between tensile strength and EMI SE for RW-M and typical shielding materials. (f) Shore D hardness of natural wood-MXene, delignified wood-MXene, RW-M, and common polymers (PLA, PP, PE, and epoxy). (g) Schematic of the abrasion–resistance test setup. (h) EMI SE of natural wood-MXene, delignified wood-MXene, and RW-M after cyclic abrasion.

visually simulated the EMI application of the RW-M through the high-frequency electromagnetic field generated by the high Tesla coil to verify its wear resistance and stability. Before wearing out, RW-M, natural wood-MXene and delignified wood-MXene could obstruct electromagnetic signal radiation, preventing the bulb from lighting up. After wearing out, natural wood-MXene and delignified wood-MXene materials were no longer block electromagnetic signal radiation, allowing the bulb to remain illuminating. In contrast, RW-M maintains its electromagnetic signal blocking capability even after 1000 abrasion cycles, preventing the bulb from lighting up (Fig. S20 in the ESM). Then we measured the wood samples before and after wear in the X-band frequency range of 8.2–12.4 dB GHz by a vector network analyzer. RW-M maintains an EMI SE at a high level of 40 dB (Fig. 5(h)), while natural wood-MXene and delignified wood-MXene materials completely lose their EMI shielding. Similarly, applying a constant voltage to the abraded samples, RW-M still exhibits an effective Joule heating effect, which is lost in natural wood-MXene and delignified wood-MXene (Figs. S21 and S22 in the ESM).

4 Conclusions

In summary, this study presents a high-strength, durable, and multifunctional RW-M through an ingenious structural design strategy. A dense 3D network of regenerated nanocellulose is constructed on the wood surface, enabling uniform deposition and penetration of Ti_3C_2 MXene nanosheets via strong hydrogen bonding and physicochemical interactions between the functional groups (–OH, –O, –F) of MXene and the cellulose scaffold. Subsequent moderate compression further enhances the interfacial compaction and interlocking, leading to the formation of a continuous and stable conductive layer. As a result, the RW-M exhibits an exceptional EMI SE of 45 dB in the X-band at a minimal thickness of 0.35 mm and a remarkable low-voltage Joule heating performance reaching 115 °C rapidly under 5 V. The robust interfacial design also imparts outstanding mechanical durability to the RW-M, which maintains structural and functional integrity under repeated mechanical abrasive conditions. Overall, this structural design strategy integrates efficient EMI shielding, rapid electrothermal response, and superior mechanical stability into a sustainable wood-based material, offering a promising platform for applications in aerospace shielding, next-generation communication devices, and extreme-environment protection. This work provides new design principles for developing high-performance, multifunctional material systems through interface-engineered integration.

Electronic Supplementary Material: Supplementary material (including detailed calculation formulas, additional characterization results (SEM, XRD, FTIR, XPS), and supplementary tables for performance comparison) is available in the online version of this article at https://doi.org/10.26599/NR.2026.94908528.

Data availability

All data needed to support the conclusions in the paper are presented in the manuscript and the Electronic Supplementary Material. The data that support the findings of this study are available from the corresponding author upon reasonable request.

Acknowledgements

We acknowledge funding support from the National Key R&D Program of China (No. 2023YFD2201404), the Fundamental Research Funds for the Central Universities (No. 2572025JT02), the key project of Natural Science Foundation of Heilongjiang Province (No. ZD2024C003), China Postdoctoral Science Foundation (No. 2020M681067), and the Special Funding Project of Postdoctoral in Heilongjiang Province (No. LBH-TZ2001).

Declaration of competing interest

The authors declare no competing financial interest.

Author contribution statement

W. T. G. conceived the idea and designed the experiments. The experiments were carried out by P. R. W. and X. F. D. W. T. G. assisted in analyzing the EMI mechanism. Z. X. Y. was instrumental in creating the 3D illustrations. X. Q. F., J. F. T., and P. J. performed material characterizations. Y. Y. L. and X. Q. L. took SEM images. Q. K. Z., X. Y. Z., Y. X. W. and R. Y. analyze the sample data. P. R. W., W. T. G., X. F. D., and Y. X. W. collectively wrote the paper. All authors commented on the final manuscript.

Use of AI statement

None.

References

[1] Wan, S. J.; Li, X.; Chen, Y.; Liu, N. N.; Du, Y.; Dou, S. X.; Jiang, L.; Cheng, Q. F. High-strength scalable MXene films through bridging-induced densification. *Science* **2021**, *374*, 96–99.

[2] Iqbal, A.; Shahzad, F.; Hantanasirisakul, K.; Kim, M. K.; Kwon, J.; Hong, J.; Kim, H.; Kim, D.; Gogotsi, Y.; Koo, C. M. Anomalous absorption of electromagnetic waves by 2D transition metal carbonitride Ti_3CNT_x (MXene). *Science* **2020**, *369*, 446–450.

[3] Zhang, Y. L.; Liu, A.; Tian, Y. Y.; Tian, Y. J.; Qi, X. S.; Qiu, H.; He, M. K.; Zhou, K.; Gu, J. W. Direct-ink-writing printed aerogels with dynamically reversible thermal management and tunable electromagnetic interference shielding. *Adv. Mater.* **2025**, *37*, 2505521.

[4] Jin, Y. H.; Han, J. H.; Park, J.; Kim, M.; Seok, S. H.; Chae, Y.; Sim, Y.; Seo, S.; Lee, H.; Wang, J. et al. Water- and oxidation-resistant MXenes for advanced electromagnetic interference shielding applications. *InfoMat* **2025**, *7*, e70034.

[5] Zhu, Y. Y.; Liu, J.; Guo, T.; Wang, J. J.; Tang, X. Z.; Nicolosi, V. Multifunctional $Ti_3C_2T_x$ MXene composite hydrogels with strain sensitivity toward absorption-dominated electromagnetic- interference shielding. *ACS Nano* **2021**, *15*, 1465–1474.

[6] Li, J. C.; Zhao, X. Y.; Wu, W. J.; Ji, X. W.; Lu, Y. L.; Zhang, L. Q. Bubble-templated rGO-graphene nanoplatelet foams encapsulated in silicon rubber for electromagnetic interference shielding and high thermal conductivity. *Chem. Eng. J.* **2021**, *415*, 129054.

[7] Wei, Q. W.; Pei, S. F.; Qian, X. T.; Liu, H. P.; Liu, Z. B.; Zhang, W. M.; Zhou, T. Y.; Zhang, Z. C.; Zhang, X. F.; Cheng, H. M. et al. Superhigh electromagnetic interference shielding of ultrathin aligned pristine graphene nanosheets film. *Adv. Mater.* **2020**, *32*, 1907411.

[8] Jia, X. C.; Shen, B.; Zhang, L. H.; Zheng, W. G. Waterproof MXene-decorated wood-pulp fabrics for high-efficiency electromagnetic interference shielding and Joule heating. *Compos. Part B: Eng.* **2020**, *198*, 108250.

[9] Zhang, Y.; Gao, Q.; Zhang, S.; Fan, X.; Qin, J. B.; Shi, X. T.; Zhang,

G. C. rGO/MXene sandwich-structured film at spunlace non-woven fabric substrate: Application to EMI shielding and electrical heating. *J. Colloid Interface Sci.* **2022**, *614*, 194–204.

[10] Liu, J. X.; Qi, S.; Wang, H. S.; Fu, C. Y.; Xu, W. L.; Su, B.; Tang, W. Y.; Xia, Z. G. Durable Fe_3O_4/PPy particle flow spun textile for electromagnetic interference shielding and joule heating. *Adv. Fiber Mater.* **2025**, *7*, 513–527.

[11] Zhao, B.; Bai, P. W.; Wang, S.; Ji, H. Y.; Fan, B. B.; Zhang, R.; Che, R. C. High-performance joule heating and electromagnetic shielding properties of anisotropic carbon scaffolds. *ACS Appl. Mater. Interfaces* **2021**, *13*, 29101–29112.

[12] Jiao, Y.; Wan, C. C.; Zhang, W. B.; Bao, W. H.; Li, J. Carbon fibers encapsulated with nano-copper: A core–shell structured composite for antibacterial and electromagnetic interference shielding applications. *Nanomaterials* **2019**, *9*, 460.

[13] Shen, Z. M.; Feng, J. C. Preparation of thermally conductive polymer composites with good electromagnetic interference shielding efficiency based on natural wood-derived carbon scaffolds. *ACS Sustain. Chem. Eng.* **2019**, *7*, 6259–6266.

[14] Liu, A.; Xu, X. S.; Qiu, H.; Guo, H.; He, M. K.; Yu, Z.; Zhang, Y. L.; Gu, J. W. Bioinspired hollow heterostructure fillers for enhanced electromagnetic interference shielding in polyimide aerogels. *InfoMat* **2025**, *7*, e70060.

[15] Liu, C.; Han, M. R.; Lin, J. P.; Liu, W.; Liu, J. R.; Zeng, Z. H. Wood biomass-derived carbon for high-performance electromagnetic wave absorbing and shielding. *Carbon* **2023**, *208*, 255–276.

[16] Huang, D. Y.; Wu, M.; Kuga, S.; Huang, Y. Graphite nanosheet-based carbon foams for electromagnetic interference shielding. *ACS Appl. Nano Mater.* **2022**, *5*, 16784–16792.

[17] Ma, X. F.; Pan, J. J.; Guo, H. T.; Wang, J. W.; Zhang, C. M.; Han, J. Q.; Lou, Z. C.; Ma, C. X.; Jiang, S. H.; Zhang, K. Ultrathin wood-derived conductive carbon composite film for electromagnetic shielding and electric heating management. *Adv. Funct. Mater.* **2023**, *33*, 2213431.

[18] Shahzad, F.; Alhabeb, M.; Hatter, C. B.; Anasori, B.; Hong, S. M.; Koo, C. M.; Gogotsi, Y. Electromagnetic interference shielding with 2D transition metal carbides (MXenes). *Science* **2016**, *353*, 1137–1140.

[19] Iqbal, A.; Sambyal, P.; Koo, C. M. 2D MXenes for electromagnetic shielding: A review. *Adv. Funct. Mater.* **2020**, *30*, 2000883.

[20] Verma, S.; Dwivedi, U.; Chaturvedi, K.; Kumari, N.; Dhangar, M.; Hashmi, S. A. R.; Singhal, R.; Srivastava, A. K. Progress of 2D MXenes based composites for efficient electromagnetic interference shielding applications: A review. *Synth. Met.* **2022**, *287*, 117095.

[21] Yun, T.; Kim, H.; Iqbal, A.; Cho, Y. S.; Lee, G. S.; Kim, M. K.; Kim, S. J.; Kim, D.; Gogotsi, Y.; Kim, S. O. et al. Electromagnetic shielding of monolayer MXene assemblies. *Adv. Mater,* **2020**, *32*, 1906769.

[22] Liu, C. Q.; Dong, J. Y.; Cheng, H. L.; He, C. G.; Zhou, B.; Huang, M.; Liu, C. T.; Feng, Y. Z. Centrifugal casting-enabled highly-oriented MXene-based layered films with dual-shielding against electromagnetic wave and infrared radiation. *Sci. China Mater.* **2026**, *69*, 395–404.

[23] Dong, J. Y.; Liu, C. Q.; Cheng, H. L.; Jiang, C. L.; Zhou, B.; Huang, M.; Liu, C. T.; Feng, Y. Z. Recent progress of $Ti_3C_2T_x$ MXene-based layered films for electromagnetic interference shielding. *J. Mater. Sci. Technol.* **2025**, *223*, 131–149.

[24] Dong, J. W.; Zhou, B.; Han, G. J.; Gao, J.; Liu, X. H.; Feng, Y. Z.; Liu, C. T.; Shen, C. Y. A multi-mode thermoregulating fabric with integrated passive/active temperature control capabilities. *Nano Res.* **2025**, *18*, 94907680.

[25] Xu, Y. H.; Pei, M.; Zhan, X.; Du, J. Y.; Zhang, D. H. Electromagnetic shielding materials of highly conductive PVA/PAA/hydrogel cross-linked with MXene. *Prog. Org. Coat.* **2024**, *194*, 108592.

[26] Xu, H. L.; Yin, X. W.; Li, X. L.; Li, M. H.; Liang, S.; Zhang, L. T.; Cheng, L. F. Lightweight Ti_2CT_x MXene/Poly(vinyl alcohol) composite foams for electromagnetic wave shielding with absorption-dominated feature. *ACS Appl. Mater. Interfaces* **2019**, *11*, 10198–10207.

[27] Liu, L. X.; Chen, W.; Zhang, H. B.; Ye, L. X.; Wang, Z. G.; Zhang, Y.; Min, P.; Yu, Z. Z. Super-tough and environmentally stable aramid. Nanofiber@MXene coaxial fibers with outstanding electromagnetic interference shielding efficiency. *Nano-Micro Lett.* **2022**, *14*, 111.

[28] Wang, J. E.; Ming, W.; Chen, L. F.; Song, T. L.; Yele, M.; Zhang, H.; Yang, L.; Sarula, G.; Liang, B. L.; Yan, L. T. et al. MoS_2 lubricate-toughened MXene/ANF composites for multifunctional electromagnetic interference shielding. *Nano-Micro Lett.* **2025**, *17*, 36.

[29] Zhao, G. X.; Sui, C.; Zhao, C. X.; Zhao, Y. S.; Cheng, G.; Li, J. J.; Wen, L.; Hao, W. Z.; Sang, Y. N.; Zhou, Y. C. et al. Super tough MXene/sodium alginate composite fiber felts integrated with outstanding electromagnetic interference shielding and heating properties. *Nano Lett.* **2024**, *24*, 8098–8106.

[30] Yu, F. W.; Liu, Q.; Ding, Y.; Zhang, W.; Ma, M. G. Multi-performance sodium alginate-based composite films for sensing and electromagnetic shielding. *Int. J. Biol. Macromol.* **2025**, *287*, 138557.

[31] He, Z. J.; Zhang, W. R.; Zhang, J.; Xie, J. L.; Su, F. F.; Li, Y. C.; Yao, D. D.; Wang, Y. D.; Zheng, Y. P. Enhancing the electromagnetic interference shielding of epoxy resin composites with hierarchically structured MXene/graphene aerogel. *Compos. Part B: Eng.* **2024**, *274*, 111230.

[32] Song, P.; Qiu, H.; Wang, L.; Liu, X. Y.; Zhang, Y. L.; Zhang, J. L.; Kong, J.; Gu, J. W. Honeycomb structural rGO-MXene/epoxy nanocomposites for superior electromagnetic interference shielding performance. *Sustainable Mater. Technol.* **2020**, *24*, e00153.

[33] Dong, X. F.; Song, R.; Wang, P. R.; Tang, J. F.; Wang, Y. X.; Shang, Y.; Xie, Y. J.; Li, J.; Song, J. W.; Gan, W. T. Multiscale engineered waste wood particles toward a sustainable, scalable, and high-performance structural material. *Adv. Funct. Mater.* **2024**, *34*, 2308361.

[34] Liu, S. L.; Yao, Y. X.; Li, X. Q.; Tang, J. F.; Dong, X. F.; Wang, Y. X.; Yin, R.; Li, J.; Xie, Y. J.; Gan, W. T. Wood ion pumps enabled by light-responsive MoS_2-decorated nanocellulosic channels. *ACS Nano* **2024**, *18*, 20353–20362.

[35] Dong, X. F.; Gan, W. T.; Shang, Y.; Tang, J. F.; Wang, Y. X.; Cao, Z. F.; Xie, Y. J.; Liu, J. Q.; Bai, L.; Li, J. et al. Low-value wood for sustainable high-performance structural materials. *Nat. Sustainability* **2022**, *5*, 628–635.

[36] Josset, S.; Orsolini, P.; Siqueira, G.; Tejado, A.; Tingaut, P.; Zimmermann, T. Energy consumption of the nanofibrillation of bleached pulp, wheat straw and recycled newspaper through a grinding process. *Nordic Pulp Pap. Res. J.* **2014**, *29*, 167–175.

[37] Tang, J. F.; Fan, X. Q.; Huang, H. Z.; Dong, X. F.; Li, X. Q.; Wang, P. R.; Yin, R.; Xie, Y. J.; Li, J.; Tan, G. et al. Biodegradable, strong, and clear wood package for plastic alternative. *Nano Res.* **2024**, *17*, 8531–8541.

[38] Xiao, S. L.; Chen, C. J.; Xia, Q. Q.; Liu, Y.; Yao, Y.; Chen, Q. Y.; Hartsfield, M.; Brozena, A.; Tu, K. K.; Eichhorn, S. J. et al. Lightweight, strong, moldable wood via cell wall engineering as a sustainable structural material. *Science* **2021**, *374*, 465–471.

[39] Lu, Z. Y.; Qi, L. H.; Chen, J. Q.; Lu, C.; Huang, J.; Chen, L.; Wu, Y. Y.; Feng, J. H.; Lin, J. Y.; Liu, Z. et al. A superstrong, decarbonizing structural material enabled by microbe-assisted cell wall engineering via a biomechanochemical process. *Sci. Adv.* **2025**, *11*, eady0183.

[40] Bai, T.; Yan, J.; Lu, J. Q.; Zhou, J.; Yao, H.; He, X. W.; Gu, S. H.; Tong, Z. H.; Shi, S. Q.; Li, J. et al. Engineering transverse cell deformation of bamboo by controlling localized moisture content. *Nat. Commun.* **2025**, *16*, 4077.

[41] Wei, Y. Y.; Hu, C. S.; Dai, Z. H.; Zhang, Y. F.; Zhang, W. W.; Lin, X. Y. Highly anisotropic MXene@Wood composites for tunable electromagnetic interference shielding. *Compos. Part A: Appl. Sci. Manuf.* **2023**, *168*, 107476.

[42] Tang, J. F.; Wu, L. P.; Fan, X. Q.; Dong, X. F.; Li, X. Q.; Xie, Y. J.; Li, J.; Rao, J. C.; Li, T.; Gan, W. T. Superstrong, sustainable, origami

wood paper enabled by dual-phase nanostructure regulation in cell walls. *Sci. Adv.* **2024**, *10*, eado5142.

[43] Falke, J. J.; Pace, R. J.; Chan, S. I. Chloride binding to the anion transport binding sites of band 3. *A 35Cl NMR study. J. Biol. Chem.* **1984**, *259*, 6472–6480.

[44] Remsing, R. C.; Swatloski, R. P.; Rogers, R. D.; Moyna, G. Mechanism of cellulose dissolution in the ionic liquid 1-*n*-butyl-3-methylimidazolium chloride: A ^{13}C and $^{35/37}$Cl NMR relaxation study on model systems. *Chem. Commun*. **2006**, 1271–1273.

[45] Zhao, X.; Wang, L. Y.; Tang, C. Y.; Zha, X. J.; Liu, Y.; Su, B. H.; Ke, K.; Bao, R. Y.; Yang, M. B.; Yang, W. Smart $Ti_3C_2T_x$ MXene fabric with fast humidity response and joule heating for healthcare and medical therapy applications. *ACS Nano* **2020**, *14*, 8793–8805.

[46] Zhang, D.; Wang, C. H.; Li, M.; Meng, W. X.; Zhang, S. P.; Yang, M. D.; Huang, X. G.; Zhang, Y. J.; Shang, Y. Y.; Cao, A. Y. Ultra-thin robust CNT@GC film integrating effective electromagnetic shielding and flexible Joule heating. *Nano Res.* **2024**, *17*, 3462–3471.

[47] Yang, P.; Xia, T.; Ghosh, S.; Wang, J. C.; Rawson, S. D.; Withers, P. J.; Kinloch, I. A.; Barg, S. Realization of 3D epoxy resin/$Ti_3C_2T_x$ MXene aerogel composites for low-voltage electrothermal heating. *2D Mater.* **2021**, *8*, 025022.

[48] Shang, T. X.; Lin, Z. F.; Qi, C. S.; Liu, X. C.; Li, P.; Tao, Y.; Wu, Z. T.; Li, D. W.; Simon, P.; Yang, Q. H. 3D macroscopic architectures from self-assembled MXene hydrogels. *Adv. Funct. Mater.* **2019**, *29*, 1903960.

[49] Yan, B. B.; Zhou, M.; Liao, X. T.; Wang, P.; Yu, Y. Y.; Yuan, J. G.; Wang, Q. Developing a multifunctional silk fabric with dual-driven heating and rapid photothermal antibacterial abilities using high-yield MXene dispersions. *ACS Appl. Mater. Interfaces* **2021**, *13*, 43414–43425.

[50] He, W. W.; Zheng, J. J.; Dong, W. P.; Jiang, S. H.; Lou, G.; Zhang, L.; Du, W. Y.; Li, Z. C.; Li, X. P.; Chen, Y. M. Efficient electromagnetic wave absorption and Joule heating via ultra-light carbon composite aerogels derived from bimetal-organic frameworks. *Chem. Eng. J.* **2023**, *459*, 141677.

[51] Yan, B. B.; Bao, X. M.; Gao, Y. L.; Zhou, M.; Yu, Y. Y.; Xu, B.; Cui, L.; Wang, Q.; Wang, P. Antioxidative MXene@GA-decorated textile assisted by metal ion for efficient electromagnetic interference shielding, dual-driven heating, and infrared thermal camouflage. *Adv. Fiber Mater.* **2023**, *5*, 2080–2098.

[52] Yan, B. B.; Huang, S. B.; Ren, Y. W.; Zhou, M.; Yu, Y. Y.; Xu, B.; Cui, L.; Wang, Q.; Wang, P. HRP-catalyzed grafting of MXene@PGA to silk fibers for visualization of dual-driven heating smart textile. *Int. J. Biol. Macromol.* **2023**, *226*, 1141–1153.

[53] Kim, S. H.; Kim, H.; Kim, N. J. Brittle intermetallic compound makes ultrastrong low-density steel with large ductility. *Nature* **2015**, *518*, 77–79.

[54] Gludovatz, B.; Hohenwarter, A.; Catoor, D.; Chang, E. H.; George, E. P.; Ritchie, R. O. A fracture-resistant high-entropy alloy for cryogenic applications. *Science* **2014**, *345*, 1153–1158.

[55] Dursun, T.; Soutis, C. Recent developments in advanced aircraft aluminium alloys. *Mater. Des. (1980–2015)* **2014**, *56*, 862–871.

[56] Li, T.; Zhai, Y.; He, S. M.; Gan, W. T.; Wei, Z. Y.; Heidarinejad, M.; Dalgo, D.; Mi, R. Y.; Zhao, X. P.; Song, J. W. et al. A radiative cooling structural material. *Science* **2019**, *364*, 760–763.

[57] Song, J. W.; Chen, C. J.; Zhu, S. Z.; Zhu, M. W.; Dai, J. Q.; Ray, U.; Li, Y. J.; Kuang, Y. D.; Li, Y. F.; Quispe, N. et al. Processing bulk natural wood into a high-performance structural material. *Nature* **2018**, *554*, 224–228.